Published in final edited form as:
Magn Reson Med. 2012 April ; 67(4): 954–964. doi:10.1002/mrm.23070.

Comparison Between Eight- and Sixteen-Channel TEM Transceive Arrays for Body Imaging at 7 Tesla

CJ Snyder[1], **L DelaBarre**[1], **S Moeller**[1], **J Tian**[1], **C Akgun**[1], **P-F Van De Moortele**[1], **PJ Bolan**[1], **K Ugurbil**[1], **JT Vaughan**[1], and **GJ Metzger**[1]

[1]Radiology, Center for Magnetic Resonance Research, Univ. Minnesota, Minneapolis, MN

Abstract

Eight- and sixteen-channel transceive stripline/TEM body arrays were compared at 7 tesla (297 MHz) both in simulation and experimentally. Despite previous demonstrations of similar arrays for use in body applications, a quantitative comparison of the two configurations has not been undertaken to date. Results were obtained on a male pelvis for assessing transmit, SNR and parallel imaging performance and to evaluate local power deposition versus transmit B_1 (B_1^+). All measurements and simulations were conducted after performing local B_1^+ phase shimming in the region of the prostate. Despite the additional challenges of decoupling immediately adjacent coils, the sixteen-channel array demonstrated improved or nearly equivalent performance to the eight-channel array based on the evaluation criteria. Experimentally, transmit performance and SNR were 22% higher for the sixteen-channel array while significantly increased reduction factors were achievable in the left-right direction for parallel imaging. Finite-difference time-domain simulations demonstrated similar results with respect to transmit and parallel imaging performance, however a higher transmit efficiency advantage of 33% was predicted. Simulations at both 3T and 7T verified the expected parallel imaging improvements with increasing field strength and showed that, for a specific B_1^+ shimming strategy employed, the sixteen-channel array exhibited lower local and global SAR for a given B_1^+.

Keywords

7 tesla; Ultrahigh field; 7T body imaging; TEM coil; Transmit/Receive Arrays; SAR

INTRODUCTION

In the last decade, substantial improvements in MRI techniques have been achieved based on the use of ultrahigh magnetic fields (7 tesla (7T) and above)(1–9). To date, most ultrahigh field applications have focused on the brain where the increased field strength has benefitted anatomic, physiologic and functional investigations. These benefits were shown to arise from field dependent gains in signal to noise ratio (SNR) (10), parallel imaging performance (11,12), and contrast mechanisms that provide unique and/or improved information. Examples in the last category include, susceptibility contrast for high resolution imaging of brain function (fMRI) (13–16), brain morphology (17,18), and vascular architecture of the venous system (19–21). Similarly, T_1 values have been shown to disperse with increasing B_0 in the brain to provide excellent T_1 contrast for anatomic imaging (22) while increases in T_1 have lead to improved arterial angiography(23,24).

Corresponding author: Gregory Metzger CMRR 2021 6th St. SE University of Minnesota Minneapolis, MN 55455-3007 gmetzger@cmrr.umn.edu phone: 612-626-2001 fax: 612-626-2004.

Imaging the human body at ultrahigh fields, however, poses substantial challenges. One of the main difficulties comes from the spatial inhomogeneities and reduced efficiency resulting from the constructive and destructive interferences between complex B_1 vectors (7). At 297 MHz (proton's Larmor frequency at 7T) the RF wavelength in body tissues are comparable to or shorter than the object of interest resulting in non-uniform excitation and receive patterns due to complex RF field interferences. These interferences reduce both the RF transmit efficiency and homogeneity, potentially increasing localized power deposition as measured by the specific absorption rate (SAR) (7,25). The ability to transmit through multiple independent channels provides the most general and flexible solution to these problems using techniques like static B_1 shimming (2,5,20) or spatially tailored RF pulses (26–28). It has been recently demonstrated that these multi-channel transmit strategies can address the complex destructive interferences and accomplish imaging even for the human torso at 7T where they pose the greatest challenge (2,4,24,29,30).

Due to the large size and distance from the body or low “filling factor,” volume arrays at 7T struggle to generate sufficient transmit B_1 due to power limitations or SAR constraints. This has, in part, lead to surface arrays being the most common method for imaging the body at 7T. With the use of surface transceiver arrays and B_1^+ shimming strategies many different body applications have been realized including those in the prostate (2), heart (4), liver (29), and uterus (30). While most of these studies use a stripline/TEM architecture similar to that originally presented in (5,31) other types of transceiver designs have also been demonstrated in the literature (32–34).

For these surface transceiver arrays, increasing the number of coils from eight to sixteen with the same overall spatial coverage was expected to provide advantages on both transmit and receive. On transmit, increasing numbers of channels should decrease the total power required to generate a given B_1^+ while simultaneously reducing SAR. On receive, gains in SNR would be expected along with increased parallel imaging performance. To investigate these potential gains with respect to increasing numbers of coils we compared the performance of similarly constructed eight-channel and sixteen-channel stripline/TEM transceive arrays for body imaging at 7T. These arrays were designed to be close fitting to the body to increase the filling factor, while the multiple transmit channels allowed for B_1^+ shimming and investigating parallel imaging performance. The two arrays were compared experimentally with respect to transmit efficiency, SNR, and parallel imaging performance in the male pelvis under conditions of a local B_1^+ phase shim. Additionally, simulations were performed to compare power deposition versus transmit performance at 7T and to assess the field dependent parallel imaging performance between 3T and 7T with the same arrays.

METHODS

RF coil and hardware

The eight-channel array consisted of a pair of four-channel stripline/TEM arrays, one located anterior and the other posterior to the torso (Fig. 1a). Four coils each were attached in parallel configuration to a flexible Polytetraflouroethylene (PTFE) plate measuring 227 × 356 × 3 mm thick. The individual coil structures were 153 mm long with a 12.7 mm wide inner conductor and a 50 mm wide outer conductor, separated by a 19 mm thick PTFE dielectric bar with a low loss tangent and a relative permittivity (ε_r) of 2.08. A 50 mm air gap separated each coil element. While similar in overall dimensions, the sixteen-channel array contained eight channels on both the anterior and posterior plates. Each individual coil had the same physical geometry as the eight-channel array, with the exception that there was no air gap between coils (Fig. 1b).

For both arrays, all coils were individually tuned to 297 MHz, and matched to a 50Ω coaxial line. Nearest neighbor coils, for both arrays, were capacitively decoupled. Fig. 2 shows the slight difference between decoupling techniques for the eight- and sixteen-channel array. In the eight-channel array, a single decoupling capacitor connecting the conductor strips was used; however in the sixteen-channel array, two decoupling capacitors were used in concert, one connecting the conductors and a second connecting the ground plates. The additional capacitive decoupling used for the sixteen-channel array was required to reach at least target isolation of 18 dB between nearest neighbor coils when loaded. All bench measurements required for coil tuning, matching and isolation were performed using a calibrated Hewlet-Packard (Palo Alto, CA) HP 4396A network analyzer together with an 85046A "S" parameter test set.

Great care needs to be taken when decoupling stripline/TEM arrays. While the coils in these arrays can be tightly packed, and since it is not possible to geometrically decouple these coils, like a loop array, coupling between neighboring coils can be significant. Currently there are limited methods for decoupling stripline/TEM arrays (35,36) with capacitive decoupling being the most prominent. During transmit, due to the B_1^+ shim, significant current and voltage drops across the decoupling capacitors are possible, the magnitude and distribution of which can vary with B_1^+ shimming. Depending on the phase set, following B_1^+ shimming, it is possible the voltage drop across the decoupling capacitor can be nearly twice the output voltage of the amplifiers with the current through the capacitor being proportional to reactive impedance of the capacitor. This needs to be considered when determining the appropriate power rating of the decoupling capacitors. For both arrays, the decoupling capacitors had a DC working voltage of 3000 V and a DC breakdown voltage of 6000 V. For consistency, the same type of capacitors used for decoupling were used for both the tuning and matching.

Imaging experiments were performed on a 7T (ω_o=297.14 MHz) magnet (Magnex Scientific, UK) interfaced to a Siemens console and whole body gradients. Parallel transmit was accomplished by a configuration where the low power output of the console was split into eight or sixteen channels through a computer controlled phase shifter and subsequently amplified by 1 kW amplifiers, one for each channel (Communications Power Corporation, Hauppauge, NY). On receive, signal amplification was accomplished with 50Ω preamps (G = 25 dB, NF = 0.9 dB at 300MHz).

Local B_1 shimming

The theory and experimental results of local B_1^+ phase shimming were previously described (2,7). In general, the objective of B_1^+ shimming can include the optimization of transmit efficiency, the creation of a homogeneous transmit B_1, reduction of local SAR or some combination of these. In this work, we used a previously characterized B_1^+ shimming method for optimizing transmit efficiency in the region of the prostate by minimizing local B_1^+ destructive interferences (2). To account for changes in exact coil positioning and geometry, B_1^+ shimming was unique for each coil, subject, and session.

Transmit B_1 and SNR Mapping

To compare transmit and receive characteristics, both B_1^+ efficiency and SNR maps were calculated. The spatially varying flip angle was calculated using the actual flip angle imaging (AFI) method (37) (TR_1 = 20 ms, TR_2 = 120 ms, TE = 3 ms, 50° nominal excitation, 128 × 128 × 16 acquisition matrix, and a 2.7 × 2.7 × 5 mm image resolution). The transmit efficiency was calculated by converting the flip angle to micro tesla and dividing that by the square root of the net input power as measured at the coil.

The receive performance was characterized by two separate gradient echo (GRE) acquisitions. The first GRE scan was used to compare SNR throughout an axial cross-section of the pelvis. To minimize the influence of varying tissue longitudinal relaxation rates on the SNR calculations, a low resolution, fully relaxed GRE acquisition was performed (TR = 6000 ms, TE = 4.08 ms, 128 × 64 acquisition matrix, 45 degree flip angle, 3 × 6 × 8 mm image resolution, 33 kHz bandwidth and a scan time of 6 min 19 s). While in general, the same fully relaxed acquisition would be desired to compare receive performance in the region of the prostate, it produced inconsistent results due to motion and variable susceptibility effects near the prostate-rectum interface. To address these issues, a higher-resolution GRE acquisition with a shorter TR and higher bandwidth was used to compare receive performance in the prostate region at the expense of being slightly T_1-weighted (TR= 76 ms, TE = 3.79 ms, 384 × 384 acquisition matrix, 1.3 × 1.3 × 5 mm image resolution, 10 degree flip angle, 4 averages, 100 kHz bandwidth and a scan time of 1 min 57 s). The T_1-weighting had minimal impact on the relative SNR due to accurate power calibration yielding similar flip angles with both coils in the prostate. To assist in evaluating coil coupling and for use in SNR calculations, data was also acquired without pulsing the RF amplifier to determine the noise-correlation matrix (38).

Maps of SNR are formed from the pseudo multiple replica method (39). Using the noise-correlation matrix, a series of 100 images of correlated noise are generated by forming an un-accelerated SENSE reconstruction. The image noise map is generated by calculating the standard deviation of the real value of a pixel through the series of noise images. The SNR is the magnitude of the image in the original reconstructed image, divided by the value of the noise standard deviation for that pixel. For both acquisitions, the GRE images were corrected for flip angle, referred to as normalized SNR (nSNR), to permit a comparison of SNR independent of B_1^+ variations.

Finite-Difference Time-Domain (FDTD) Simulations

Numerical Maxwell solutions of the eight- and sixteen-channel stripline transceiver arrays were calculated in an anatomically correct human body model (Duke from Virtual Family (40)) using XFDTD (Remcom Inc., State College, PA) to estimate power deposition (SAR), assess theoretical transmit, and parallel imaging performance. The body and both arrays were modeled at an isotropic resolution of 5 mm. Each coil was driven by one voltage source and tuned to proton's Larmor frequency at 7T. For a given array, all coils were simulated individually, normalized for net input power, and then optimally combined using the same B_1^+ shimming methods employed in vivo. Peak 10 gram averaged SAR in the body was determined after B_1^+ shimming. The ratio of peak local SAR (normalized to 1 W input power) divided by the square of the average $\mu T/W^{0.5}$ generated in the prostate was used as a further combined metric of coil and B_1^+ shimming performance. Theoretical parallel imaging performance was also calculated from the simulated data for comparison with 7T experimental results while the same models were run at 128 MHz to estimate geometry factors for the same array designs at 3T.

Parallel Imaging Performance

Experimental determination of parallel imaging performance for encoding spatial information was compared against simulated results for both arrays at 7T by calculating geometry factors (g-factors) under various parallel imaging conditions. Experimental calculations were performed on data acquired in vivo with a 3D-FLASH sequence (TR = 3.11 ms, TE = 1.25 ms, 20 slices, 400 × 400 × 160 mm field of view, 0.78 × 0.78 × 5.0 mm resolution and 32 s acquisition time), and simulated calculations were based on calculated B_1^- fields from the previously described FDTD simulations. Parallel imaging performance,

in the form of mean and maximum g-factors, were calculated on a central slice following methods presented by Pruessmann et al. (38).

Additionally, using this 3D FLASH sequence, 1-D reduction factors of 2, 4, and 8 were acquired in the left-right direction reducing the acquisition time to 16 s, 8 s and 4 s respectively. In this case, a full resolution image (R=1) acquired separately was used to calculate a 5×4 GRAPPA kernel, which in turn, was used to reconstruct the accelerated images (R>1). This meant that effectively 512 auto-calibration scan (ACS) lines were used, although far fewer would be necessary to estimate the reconstruction kernel. By performing the reconstruction in this manner, the reconstructed images are not biased by the specific GRAPPA kernel employed, thereby reflecting only the g-factor noise amplification.

RESULTS

RF coil

Table 1 shows the unloaded and loaded Q values for both arrays and the isolation between nearest-neighbor next-nearest neighbor coils for both the unloaded and loaded case. For comparison, loaded and unloaded Q values for a single element TEM coil, which is the building block for both arrays, is also reported in table 1. Both arrays show lower unloaded Q values then the single element, this attributed to the coupling to both the nearest neighbor and next-nearest neighbor coupling. The large standard deviation in the unloaded Q's is due to the physical placement of the coils in the array; medial coils had noticeably lower Q's then the lateral coils.

In contrast to the bench measurements, fig. 1e and 1f show the covariance of the noise for the receiver chain. In the eight-channel array, the maximum amount of coupling between any two channels was between coils 4 and 5 (15dB isolation). Similarly in the sixteen-channel array maximum coupling between any two channels occurs between coils 10 and 12 (17dB isolation).

B_1^+ Shimming

The results of local B_1^+ shimming for the sixteen-channel array are shown in Fig. 3. Prior to B_1^+ shimming, all coils were set to have an equal transmit phase (Fig. 3a); the image inhomogeneity and signal voids are due primarily to the complex destructive interference patterns of the transmit B_1 (Fig. 3c). By calculating the correct phases (Fig. 3d), the RF efficiency can be greatly increased over a specified target, in this case, the prostate (Fig. 3b). For such a small target near the center of the coil, even though not explicitly optimized, this B_1^+ shimming method greatly increases homogeneity over the same region. A theoretical discussion of local B_1^+ shimming at 7T and examples of the B_1^+ shimming in the prostate using the eight-channel array can be found in Metzger et al. (2). Figures 1c and 1d show the axial gradient echo images acquired following B_1^+ shimming in the prostate on the eight- and sixteen-channel arrays, respectively.

Experimental Transmit and Receive Performance

After B_1^+ shimming in the prostate, transmit B_1 magnitude maps of the lower pelvis were calculated using the AFI method to assess transmit performance of both arrays, Fig. 4a and 4b (37). In the case shown, the transmit performance in the prostate for the eight-channel and sixteen-channel arrays were 0.169 ± 0.017 and 0.206 ± 0.025 $\mu T/W^{0.5}$, respectively (Table 2).

The nSNR images calculated from the high resolution GRE images are shown for both arrays, Fig. 4c and 4d. The nSNR in the region of the prostate was 22% higher for the

sixteen-channel array compared to the eight-channel. To assess the receive performance of the two arrays across the pelvis, the fully relaxed SNR acquisition was used to generate nSNR images independent of T_1 effects. A histogram of all the voxels within the two nSNR images for the eight- and sixteen-channel arrays are shown in Fig. 5. These nSNR maps demonstrate the improved receive performance and uniformity of the sixteen-channel array especially near the periphery.

Simulated B_1^+ and SAR

The simulated transmit performance for both arrays along with the normalized 10 gram peak local SAR and whole body SAR after B_1^+ shimming are given in table 2. Figures 6a and 6b show the position of the ROI used for B_1^+ shimming and the region over which the mean and standard deviations of B_1^+ were determined. The simulated transmit performance in the prostate for the eight-channel and sixteen-channel arrays were 0.202 ± 0.018 and 0.267 ± 0.022 $\mu T/W^{0.5}$, respectively (Table 2).

Figures 6c and 6d show the 10-gram averaged SAR for the eight-channel and sixteen-channel array, respectively. The yellow arrow in figure 6c and 6d indicate the location of maximum SAR in each case. To characterize the performance of each array, with the current B_1^+ shim solution, the ratio of the maximum local SAR per unit input power (SAR/W) to the squared average B_1^+ per watt ($\mu T^2/W$) in the target region was calculated and shown in Table 2. This ratio was $0.36/(0.20)^2 = 8.7$ and $0.34/(0.27)^2 = 4.8$ $W/kg/\mu T^2$ for the eight-channel and sixteen-channel arrays, respectively. Similar results for the whole body SAR are also reported in Table 2.

Parallel Imaging Performance

For a range of reduction factors, Table 3 shows the g-factors for the eight-channel array from the *in vivo* data, as well as modeled data for both 7T and 3T. Similarly, table 4 shows the same for the sixteen-channel array. In the tables, left-right refers to reduction factors along the x-axis and anterior-posterior refers to reduction factors along the y-axis. The "mean" represents the average g-factors from the given slices while the "max" values represent the worst case within the slice for this spatially varying parameter. Based on imaging results, a mean g-factor ≤ 1.6 produced high quality images with only nominal aliasing. Therefore, using 1.6 as the upper limit for the allowable mean g-factor, "x" by "y" reduction factors in vivo of 4 × 1 and 4 × 2 were achievable with the eight-channel array while the sixteen-channel array reached reduction factors of 8 × 1 and 6 × 2.

Tables 3 and 4 show the extremely close correspondence at 7T between simulated and measured g-factors for the eight- and sixteen-channel arrays, thus indicating that simulations can accurately model the complex B_1^- patterns present at ultrahigh field strengths. This conclusion permits us to compare 3T versus 7T performance using simulations for a coil of the same dimensions and geometry. In these simulations, higher reduction factors with acceptable performance (mean g-factors < ~1.6 and max < ~3) were observed for the sixteen-channel array at 7T compared to 3T.

Maps of 1/g-factors from in vivo data for accelerations in the left-right direction are shown for the eight- and sixteen-channel arrays in Fig. 7 while Fig. 8 shows the GRAPPA reconstructed images from the same acquisitions. As expected, the eight-channel cannot support 1-D reduction factors greater than four, whereas the sixteen-channel array provides images with virtually undetectable image degradation for reduction factors as high as eight (Fig. 8). Even with somewhat larger image degradation, such images can still be acceptable for many applications where time resolution is critical, such as dynamic contrast enhanced

studies where accurately measuring the contrast bolus can improve pharmacokinetic modeling (41).

DISCUSSION

Although preliminary studies have shown the feasibility of imaging the torso at 7T, further RF coil and array design developments can improve performance. At lower field strengths, a large single-channel body coil is often used for excitation and combined with local receive-only surface coils. Vaughan et al (3) have previously shown that the single channel volume coil is impractical at 7T because the reduced wavelengths in the human body at 300 MHz create substantial destructive interferences resulting in RF shading (7). While this phenomenon can be seen at lower field strengths, adjusting the phase and current on the individual current carrying rungs of the body coil once can create a “universal” RF shim adequate for most patients (42). This is not the case at 7T where body imaging requires the use of multiple transmit arrays that allow subject-dependent and region-specific optimization of B_1^+.

RF Array

In this paper, an eight- and a sixteen-channel TEM/Stripline array were compared with respect to transmit and receive performance through in vivo imaging and simulation. A TEM array design was chosen because of the compact physical size and the known efficiency of TEM arrays at high fields (5,42). The two arrays were compared on transmit, receive, SAR and parallel imaging performance.

Both arrays were designed and constructed to be nearly identical, where the physical dimensions of the individual coils as well as the overall size of the arrays were nearly identical. Both arrays were constructed out of identical materials and built, tuned and matched in the same manner. The main difference between the two arrays is the method of decoupling. When loaded, the eight-channel array was able to achieve greater then 18dB isolation between nearest neighbor coils by using capacitive decoupling on the conductors alone. A similar level of isolation was not achievable on the sixteen-channel array without the addition of decoupling capacitors on the ground plates. While ground plate decoupling capacitors could have been added to the eight-channel array, it was considered unnecessary. Decoupling capacitors are lossy, can create parasitic current loops, field perturbing loops, and potentially destroy the desired field profile of the coil, therefore the least amount of decoupling possible to achieve greater than 18dB of isolation between nearest neighboring channels was used.

Individual coil geometries were optimized, based on previous 7T transcieve coils and arrays, to maximize penetration while minimizing crosstalk. Kumar and Bottomley found the center conductor's width to only weakly determine the intrinsic single to noise ratio of a stripline/TEM or planer strip coil, with the optimal conductor strip width equal to dielectric width (43). We chose a slightly smaller width to dielectric height ratio to reduce the coupling between neighboring coils.

Transmit B_1 Performance

The experimentally measured B_1^+ performance and transmit efficiency advantage of the sixteen-channel array were lower than those predicted by simulation despite performing in vivo studies on a subject with similar body characteristics and dimensions as the body model. While achieving exact correspondence between simulation and in vivo measurements would be desirable, there are several factors which can account for the majority of the observed differences in our study. First, while we do include component

losses for the capacitors and conductors in the simulation, the coil efficiency is still overestimated when compared to the physical coil. Because of the high density of coils and additional decoupling required, the overestimation is greater for the sixteen-channel array thus reducing the transmit efficiency gains predicted by simulation. Second, the power used to normalize the B_1^+ when characterizing transmit efficiency is obtained in simulation from the net input power, all of which reaches the coil. Experimentally however, we use the incident power to normalize the measured B_1^+ where in reality some is reflected. Reflected power can vary depending on the coil specific matching and on the specific B_1^+ shim applied. Underestimating the coil losses and overestimating the power that enters the coil experimentally results in a lower transmit efficiency however, it also yields a conservative estimate of local and global SAR.

Impact of Coil Number on SAR and B_1^+ Optimization

In the work by Lattanzi et al., the principle of ultimate intrinsic SAR (the lowest possible SAR independent of coil design) was used to compare optimization strategies using various SAR and transmit B_1^+ constraints (44). With the combined goal of obtaining a uniform B_1^+ with global SAR reduction, Lattanzi demonstrated that global SAR approaches the ultimate intrinsic SAR as the number of transmit channels increase. Even though in the current study we optimized our transmit B_1^+ to minimize destructive interferences with a much simpler phase based approach, a reduction in global (36%) as well as local (45%) SAR was observed with the sixteen-channel array after normalizing by B_1^+ (Table 2).

Many factors affect SAR and B_1^+ performance beyond the specific configuration of an array including the size, location, and optimization goal of the B_1^+ shimming strategy as well as the size, shape, and composition of a given subject. Beyond the simple B_1^+ shimming strategy employed in this study, the phases and amplitudes could be optimized to generate a nearly equivalent B_1^+ and similar homogeneity with substantial decreases in maximum local SAR. For example, Van den Bergen et al. demonstrated through simulation that B_1 shimming can be performed while explicitly optimizing for SAR reduction to great effect at 7T when using a twelve-channel TEM volume array (45). Future studies are warranted to investigate the impact of arrays with varying numbers of coils on such optimization strategies.

Along with local SAR, the available power also greatly limits which B_1^+ shimming strategies can be practically employed. If a SAR reduction or homogeneity solution were used, power efficiency can drop dramatically (45). For body applications, even when using the power efficient phase-only approach employed in this work on a small region of interest, it is difficult to generate the peak B_1^+ desired for certain applications. Therefore, employing less efficient strategies become increasingly challenging. This problem is exacerbated by the limited total power available on most multi-transmit channel 7 tesla systems. On most multi-transmit channel 7 tesla systems, each channel is driven by a 1 kW amplifier. Even modest increases in transmit efficiency, as observed experimentally in this study with the sixteen-channel array, can benefit applications which require high peak B_1^+ such as spectroscopy and inversion prepared imaging sequences.

Parallel Imaging Performance

Parallel imaging performance is expected to improve as the relative object size (object dimensions versus the wavelength) increases (11). The results presented in this paper were first shown by Snyder et al (31) and closely follow Wiesinger's (11) theoretical results that large reduction factors can be obtained in the human pelvis at higher field strengths with a moderate number of receiver coils. There is clearly a large gain achieved with sixteen-

channels compared to eight-channels at 7T. With the sixteen-channel array an 8×1 reduction can be attained with excellent average and maximum g-factors.

Tables 3 and 4 show substantial agreement between our experimental data at 7T and the g-factors predicted by simulation. This provides confidence that modeling can be used to predict the g-factors for these arrays at other field strengths. Tables 3 and 4 also show the predicted g-factors for identical eight- and sixteen-channel arrays at 3T. There is little difference in parallel imaging performance between 3T and 7T for the eight-channel array. This is likely because the coils are placed sufficiently far apart in the eight-channel design to yield spatially distinct sensitivity profiles at both field strengths. However, with the sixteen-channel array, further significant gains in parallel imaging performance are achieved at 7T which are not realized at 3T. This would be expected based on the relative object size (11,12).

The improved parallel imaging performance for the sixteen-channel array is primarily in the left-right direction which is optimal for many imaging studies of the torso. For an axial orientation, some applications in the torso take advantage of a reduced field of view in the anterior-posterior (AP) direction when phase encoding in that same direction. Performing the phase encoding in this manner allows the spatial resolution to be maintained while reducing the scan time as fewer phase encode lines are required. However, phase encoding in the AP direction is susceptible to motion artifacts from respiration, bowel and other sources. This is especially true for the arrays described in this work because of the high intensity and inhomogeneity of the transmit and receive B_1 fields immediately adjacent to the coil. In the case of prostate imaging, most axial data sets are acquired with a left-right phase encode to minimize artifacts in the region of interest resulting from the abdominal wall (or the endorectal coil if present). Dynamic contrast enhanced MRI is a typical example, which typically uses parallel imaging acceleration in the left-right direction to increase the temporal resolution for resolving the arterial input function and the tissue time courses. For non-contrast enhanced renal angiography at 7T, the phase encode direction is also in the left-right direction to avoid artifacts from bowel motion (46).

Finally, while not experimentally demonstrated in this work, these RF coil arrays can be used to generate spatially targeted and accelerated RF pulses using parallel transmit methods. For the same reasons the sixteen-channel array outperforms the eight-channel array in parallel imaging on the receive side, it would be expected to lead to higher “accelerations” in transmission as well.

CONCLUSION

Eight- and sixteen -channel stripline/TEM surface arrays were compared for body imaging at 7T both through simulation and experimentation. For this comparison local phase based B_1^+ shimming was employed to minimize the destructive interferences in a region surrounding the prostate as a basis for comparing transmit, receive and parallel imaging performance as well as local and global SAR. Experimentally, the sixteen-channel array demonstrated a 22% increase in transmit and receive performance in the target anatomy of the prostate. Advantages in receive performance increased for the sixteen-channel array when moving from the center of the body towards the periphery (closer to the coil elements). While the gain in transmit and receive performance are significant for the sixteen-channel array, the most substantial advantages are arguably the greatly improved parallel imaging performance and the potential for reducing local and global SAR.

The issues that arise from positioning the stripline/TEM coils immediately adjacent to each other in the sixteen-channel array have to be considered along with the realized and potential

advantages. In contrast, the increased coil spacing in the eight-channel array reduces coupling between channels and decreases complexity in construction and optimization. Determining which coil to use at a given site and for a particular application will depend on several factors including the RF amplifier configuration, requirements on peak B_1^+ and homogeneity and the availability of B_1^+ optimization methods and parallel transmit capabilities.

Acknowledgments

Funding for this work was provided by the National Institutes of Health (NIH) grants P41-RR008079, R01-EB007327, R01-EB006835, and R01-EB000895. The original acquisition of the 7 tesla system was funded by the Keck Foundation, NSF grant 9907842 and NIH grant S10-RR1395. We would also like to acknowledge Gregor Adriany, Peter Anderson and John Strupp for their scientific conversations and contributions.

REFERENCES

1. Krug R, Carballido-Gamio J, Banerjee S, Stahl R, Carvajal L, Xu D, Vigneron D, Kelley DA, Link TM, Majumdar S. In vivo bone and cartilage MRI using fully-balanced steady-state free-precession at 7 tesla. Magn Reson Med. 2007; 58(6):1294–1298. [PubMed: 17957777]
2. Metzger GJ, Snyder C, Akgun C, Vaughan T, Ugurbil K, Van de Moortele PF. Local B1+ shimming for prostate imaging with transceiver arrays at 7T based on subject-dependent transmit phase measurements. Magn Reson Med. 2008; 59(2):396–409. [PubMed: 18228604]
3. Vaughan JT, Snyder CJ, DelaBarre LJ, Bolan PJ, Tian J, Bolinger L, Adriany G, Andersen P, Strupp J, Ugurbil K. Whole-body imaging at 7T: preliminary results. Magn Reson Med. 2009; 61(1):244–248. [PubMed: 19097214]
4. Snyder CJ, DelaBarre L, Metzger GJ, van de Moortele PF, Akgun C, Ugurbil K, Vaughan JT. Initial results of cardiac imaging at 7 Tesla. Magn Reson Med. 2009; 61(3):517–524. [PubMed: 19097233]
5. Adriany G, Van de Moortele PF, Wiesinger F, Moeller S, Strupp JP, Andersen P, Snyder C, Zhang X, Chen W, Pruessmann KP, Boesiger P, Vaughan T, Ugurbil K. Transmit and receive transmission line arrays for 7 Tesla parallel imaging. Magn Reson Med. 2005; 53(2):434–445. [PubMed: 15678527]
6. Brunner DO, De Zanche N, Frohlich J, Paska J, Pruessmann KP. Travelling-wave nuclear magnetic resonance. Nature. 2009; 457(7232):994–998. [PubMed: 19225521]
7. Van de Moortele PF, Akgun C, Adriany G, Moeller S, Ritter J, Collins CM, Smith MB, Vaughan JT, Ugurbil K. B(1) destructive interferences and spatial phase patterns at 7 T with a head transceiver array coil. Magn Reson Med. 2005; 54(6):1503–1518. [PubMed: 16270333]
8. van Elderen SG, Versluis MJ, Webb AG, Westenberg JJ, Doornbos J, Smith NB, de Roos A, Stuber M. Initial results on in vivo human coronary MR angiography at 7 T. Magn Reson Med. 2009; 62(6):1379–1384. [PubMed: 19859918]
9. Chang G, Friedrich KM, Wang L, Vieira RL, Schweitzer ME, Recht MP, Wiggins GC, Regatte RR. MRI of the wrist at 7 tesla using an eight-channel array coil combined with parallel imaging: preliminary results. J Magn Reson Imaging. 31(3):740–746. [PubMed: 20187221]
10. Vaughan JT, Garwood M, Collins CM, Liu W, DelaBarre L, Adriany G, Andersen P, Merkle H, Goebel R, Smith MB, Ugurbil K. 7T vs. 4T: RF power, homogeneity, and signal-to-noise comparison in head images. Magn Reson Med. 2001; 46(1):24–30. [PubMed: 11443707]
11. Wiesinger F, Van de Moortele PF, Adriany G, De Zanche N, Ugurbil K, Pruessmann KP. Parallel imaging performance as a function of field strength--an experimental investigation using electrodynamic scaling. Magn Reson Med. 2004; 52(5):953–964. [PubMed: 15508167]
12. Ohliger MA, Grant AK, Sodickson DK. Ultimate intrinsic signal-to-noise ratio for parallel MRI: electromagnetic field considerations. Magn Reson Med. 2003; 50(5):1018–1030. [PubMed: 14587013]
13. Yacoub E, Harel N, Ugurbil K. High-field fMRI unveils orientation columns in humans. Proc Natl Acad Sci U S A. 2008; 105(30):10607–10612. [PubMed: 18641121]

14. Yacoub E, Shmuel A, Logothetis N, Ugurbil K. Robust detection of ocular dominance columns in humans using Hahn Spin Echo BOLD functional MRI at 7 Tesla. Neuroimage. 2007; 37(4):1161–1177. [PubMed: 17702606]
15. Yacoub E, Van De Moortele PF, Shmuel A, Ugurbil K. Signal and noise characteristics of Hahn SE and GE BOLD fMRI at 7 T in humans. Neuroimage. 2005; 24(3):738–750. [PubMed: 15652309]
16. Yacoub E, Duong TQ, Van De Moortele PF, Lindquist M, Adriany G, Kim SG, Ugurbil K, Hu X. Spin-echo fMRI in humans using high spatial resolutions and high magnetic fields. Magn Reson Med. 2003; 49(4):655–664. [PubMed: 12652536]
17. Yao B, Li TQ, Gelderen P, Shmueli K, de Zwart JA, Duyn JH. Susceptibility contrast in high field MRI of human brain as a function of tissue iron content. Neuroimage. 2009; 44(4):1259–1266. [PubMed: 19027861]
18. Duyn JH, van Gelderen P, Li TQ, de Zwart JA, Koretsky AP, Fukunaga M. High-field MRI of brain cortical substructure based on signal phase. Proc Natl Acad Sci U S A. 2007; 104(28): 11796–11801. [PubMed: 17586684]
19. Burgess RE, Yu Y, Christoforidis GA, Bourekas EC, Chakeres DW, Spigos D, Kangarlu A, Abduljalil AM, Robitaille PM. Human leptomeningeal and cortical vascular anatomy of the cerebral cortex at 8 Tesla. J Comput Assist Tomogr. 1999; 23(6):850–856. [PubMed: 10589558]
20. Vaughan T, DelaBarre L, Snyder C, Tian J, Akgun C, Shrivastava D, Liu W, Olson C, Adriany G, Strupp J, Andersen P, Gopinath A, van de Moortele PF, Garwood M, Ugurbil K. 9.4T human MRI: preliminary results. Magn Reson Med. 2006; 56(6):1274–1282. [PubMed: 17075852]
21. Adriany G, Van de Moortele PF, Ritter J, Moeller S, Auerbach EJ, Akgun C, Snyder CJ, Vaughan T, Ugurbil K. A geometrically adjustable 16-channel transmit/receive transmission line array for improved RF efficiency and parallel imaging performance at 7 Tesla. Magn Reson Med. 2008; 59(3):590–597. [PubMed: 18219635]
22. Rooney WD, Johnson G, Li X, Cohen ER, Kim SG, Ugurbil K, Springer CS Jr. Magnetic field and tissue dependencies of human brain longitudinal 1H2O relaxation in vivo. Magn Reson Med. 2007; 57(2):308–318. [PubMed: 17260370]
23. Kang CK, Park CW, Han JY, Kim SH, Park CA, Kim KN, Hong SM, Kim YB, Lee KH, Cho ZH. Imaging and analysis of lenticulostriate arteries using 7.0-Tesla magnetic resonance angiography. Magn Reson Med. 2009; 61(1):136–144. [PubMed: 19097221]
24. Van de Moortele PF, Auerbach EJ, Olman C, Yacoub E, Ugurbil K, Moeller S. T1 weighted brain images at 7 Tesla unbiased for Proton Density, T2* contrast and RF coil receive B1 sensitivity with simultaneous vessel visualization. Neuroimage. 2009; 46(2):432–446. [PubMed: 19233292]
25. Yang QX, Wang J, Zhang X, Collins CM, Smith MB, Liu H, Zhu XH, Vaughan JT, Ugurbil K, Chen W. Analysis of wave behavior in lossy dielectric samples at high field. Magn Reson Med. 2002; 47(5):982–989. [PubMed: 11979578]
26. Katscher U, Bornert P, Leussler C, van den Brink JS. Transmit SENSE. Magn Reson Med. 2003; 49(1):144–150. [PubMed: 12509830]
27. Grissom W, Yip CY, Zhang Z, Stenger VA, Fessler JA, Noll DC. Spatial domain method for the design of RF pulses in multicoil parallel excitation. Magn Reson Med. 2006; 56(3):620–629. [PubMed: 16894579]
28. Zelinski AC, Wald LL, Setsompop K, Alagappan V, Gagoski BA, Goyal VK, Adalsteinsson E. Fast slice-selective radio-frequency excitation pulses for mitigating B+1 inhomogeneity in the human brain at 7 Tesla. Magn Reson Med. 2008; 59(6):1355–1364. [PubMed: 18506800]
29. Styczynski-Snyder, AL.; Snyder, CJ.; DelaBarre, L.; Van de Moortele, P-F.; Vaughan, JT.; Ugurbil, K.; Garwood, M.; Bolan, PJ. Preliminary Experience with Liver MRI and 1H MRS at 7 tesla. 16th Annual Meeting of ISMRM; Berlin. 2007. p. 729
30. Styczynski Snyder, AL.; Snyder, C.; Van de Moortele, P-F.; DelaBarre, L.; Haddidin, IS.; Truskinovky, A.; Vaughan, JT.; Ugurbil, K.; Garwood, M.; Michaeli, S. Endometrial imaging at high magnetic fields: feasibility of *in vivo* studies at 7T. 16th Annual Meeting of ISMRM; Berlin. 2007. p. 573

31. Snyder, C.; DelaBarre, L.; Van de Moortele, P-F.; Styczynski Snyder, A.; Akgun, C.; Tian, J.; Metzger, G.; Ugurbil, K.; Vaughan, J. Stripline/TEM Transceiver Array for 7T Body Imaging. 16th Annual Meeting of ISMRM; Berlin. 2007. p. 164
32. Orzada, S.; Maderwald, S.; Oehmigen, M.; Ladd, M.; Solbach, K.; Bitz, A. An 8-Channel TX, 16-Channel Flexible Body Coil at 7 Tesla Using Both Branches of Centrally Fed Strip Lines as Individual Receive Elements. 18th Annual Meeting of ISMRM; Stockholm. 2010. p. 641
33. Raaijmakers, A.; Ipek, O.; Klomp, D.; Kroeze, H.; van de Bank, B.; Boer, V.; Harvey, P.; Possanzini, C.; Lagendijk, J.; van den Berg, N. High-Field Imaging at Low SAR: Tx/Rx Prostate Coil Array Using Radiative Elements for Efficient Antenna-Patient Power Transfer. 18th Annual Meeting of ISMRM; Stockholm. 2010. p. 48
34. Umutlu L, Orzada S, Kinner S, Maderwald S, Brote I, Bitz AK, Kraff O, Ladd SC, Antoch G, Ladd ME, Quick HH, Lauenstein TC. Renal imaging at 7 Tesla: preliminary results. Eur Radiol. 21(4):841–849. [PubMed: 20872006]
35. Wang, J. A Novel Method to Reduce the Signal Coupling of Surface Coils for MRI. 4th Annual Meeting of ISMRM; New York. 1996. p. 1434
36. Vaughan, JT.; Snyder, CJ.; DelaBarre, L.; Tian, J.; Adriany, G.; Anderson, P.; Strupp, J.; Ugurbil, K. Clinical Imaging at 7T with a 16 Channel Whole Body Coil and 32 Receive Channels. 17th Annual Meeting of ISMRM; Honolulu. 2009. p. 391
37. Yarnykh VL. Actual flip-angle imaging in the pulsed steady state: a method for rapid three-dimensional mapping of the transmitted radiofrequency field. Magn Reson Med. 2007; 57(1):192–200. [PubMed: 17191242]
38. Pruessmann KP, Weiger M, Scheidegger MB, Boesiger P. SENSE: sensitivity encoding for fast MRI. Magn Reson Med. 1999; 42(5):952–962. [PubMed: 10542355]
39. Robson PM, Grant AK, Madhuranthakam AJ, Lattanzi R, Sodickson DK, McKenzie CA. Comprehensive quantification of signal-to-noise ratio and g-factor for image-based and k-space-based parallel imaging reconstructions. Magn Reson Med. 2008; 60(4):895–907. [PubMed: 18816810]
40. Christ A, Kainz W, Hahn EG, Honegger K, Zefferer M, Neufeld E, Rascher W, Janka R, Bautz W, Chen J, Kiefer B, Schmitt P, Hollenbach HP, Shen J, Oberle M, Szczerba D, Kam A, Guag JW, Kuster N. The Virtual Family--development of surface-based anatomical models of two adults and two children for dosimetric simulations. Phys Med Biol. 55(2):N23–38. [PubMed: 20019402]
41. Henderson E, Rutt BK, Lee TY. Temporal sampling requirements for the tracer kinetics modeling of breast disease. Magn Reson Imaging. 1998; 16(9):1057–1073. [PubMed: 9839990]
42. Vaughan JT, Adriany G, Snyder CJ, Tian J, Thiel T, Bolinger L, Liu H, DelaBarre L, Ugurbil K. Efficient high-frequency body coil for high-field MRI. Magn Reson Med. 2004; 52(4):851–859. [PubMed: 15389967]
43. Kumar A, Bottomley PA. Optimizing the intrinsic signal-to-noise ratio of MRI strip detectors. Magn Reson Med. 2006; 56(1):157–166. [PubMed: 16724302]
44. Lattanzi R, Sodickson DK, Grant AK, Zhu Y. Electrodynamic constraints on homogeneity and radiofrequency power deposition in multiple coil excitations. Magn Reson Med. 2009; 61(2):315–334. [PubMed: 19165885]
45. van den Bergen B, Stolk CC, Berg JB, Lagendijk JJ, Van den Berg CA. Ultra fast electromagnetic field computations for RF multi-transmit techniques in high field MRI. Phys Med Biol. 2009; 54(5):1253–1264. [PubMed: 19182321]
46. Metzger, G.; Simonson, J.; Bi, X.; Weale, P.; Zuehlsdorff, S.; Auerbach, E.; Ugurbil, K.; Van de Moortele, P-F. Initial Experience with Non-Contrast Enhanced Renal Angiography at 7.0 Tesla. 18th Annual Meeting of ISMRM; Stockholm. 2010. p. 401

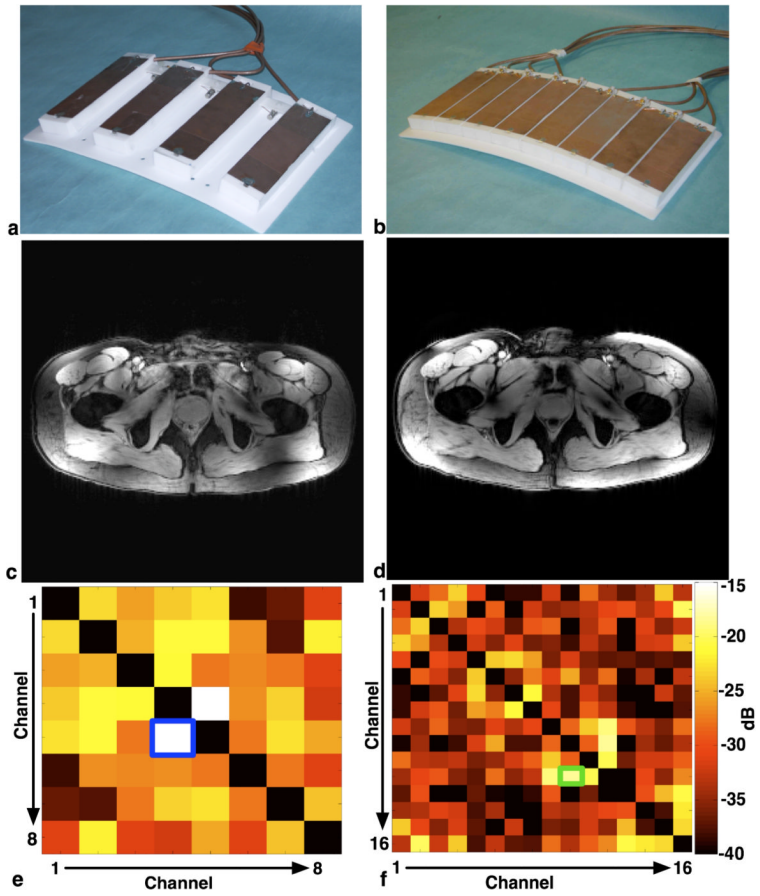

Fig. 1.

Anterior plate of the eight-channel (a) and sixteen-channel (b) arrays and gradient recalled echo images (c) and (d) show the spatial coverage, in the axial plane, of the eight- and sixteen-channel arrays, respectively. The corresponding covariance of the noise (38) of the receiver chain, (e) and (f) respectively. The blue box in (e) shows the greatest coupling occurs between channels four and five in the eight-channel array while the green box in (f) shows the greatest coupling occurring between channels ten and twelve in the sixteen-channel array.

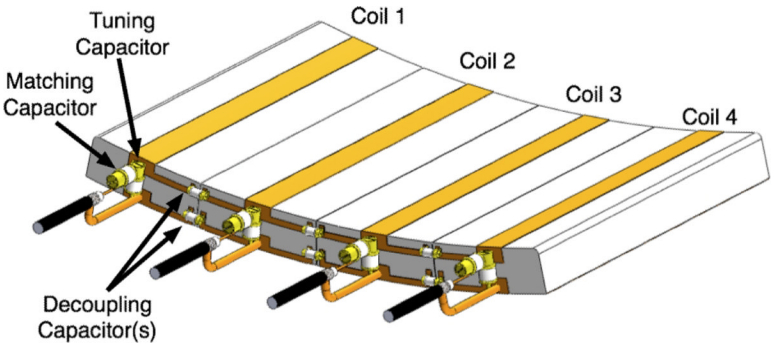

Fig. 2.

An example of a four-channel stripline/TEM transcieve array showing the placement of the tuning, matching, and decoupling capacitors. In the actual eight-channel array there would be a 5cm air gaps between the coils and only require the conductor strip decoupling. All tuning, matching and decoupling capacitors are 1–10 pF variable capacitors.

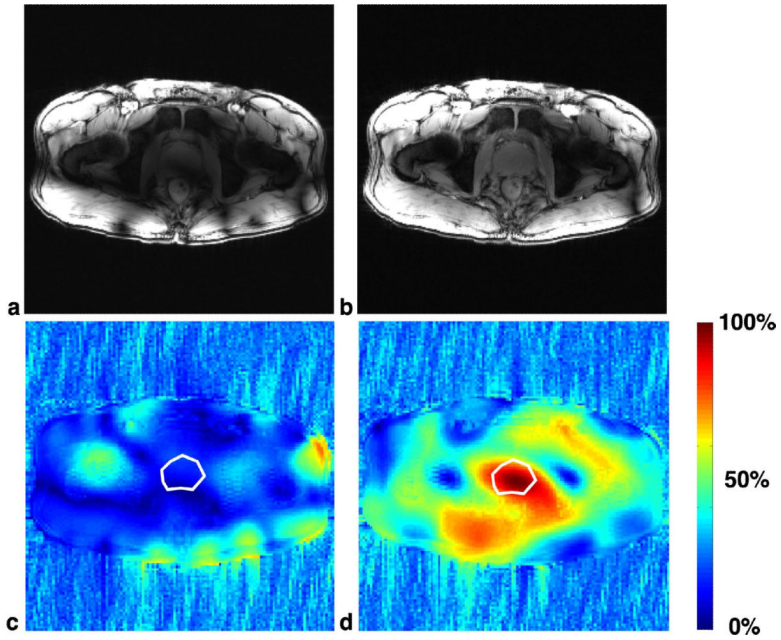

Fig. 3.

Representative B_1^+ shimming results in the sixteen-channel array. (a) and (b) are axial gradient recalled echo scout images before and after local B_1^+ shimming, respectively. The areas of signal dropout, or RF shading, in (a) are primarily due to complex destructive interference of the B_1^+ between transmit channels. (c) and (d) show the percent of available B_1^+ (magnitude of the sum over the sum of the magnitude of all B_1^+ fields), before and after B_1 shimming, respectively; the white polygon is the region of interest, the prostate, where the transmit efficiency was optimized. Prior to B_1^+ shimming, most of the B_1^+ from individual coils was adding destructively resulting in an available B_1^+ of 20% (c). After B_1^+ shimming, transmit efficiency is greatly increased (d).

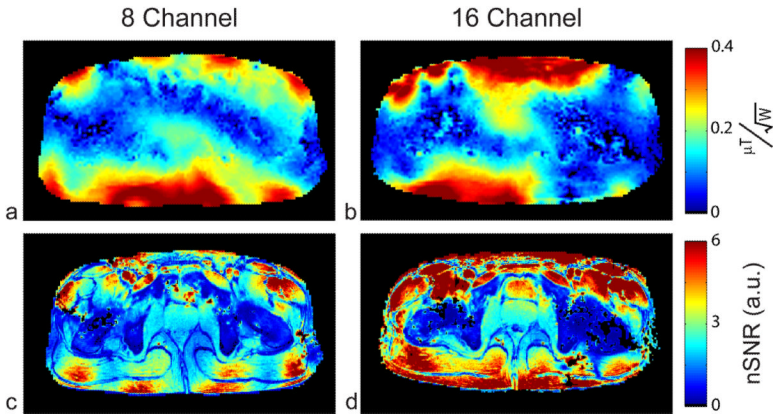

Fig. 4.

B_1^+ maps normalized by input power for the eight- (a) and sixteen-channel (b) arrays. SNR normalized by B_1^+ (nSNR) for the eight (c) and sixteen-channel (d) arrays generated from the high resolution GRE acquisition. The transmit performance of the sixteen-channel array is 22% higher; the nSNR in the prostate is also 22% higher with the sixteen-channel array.

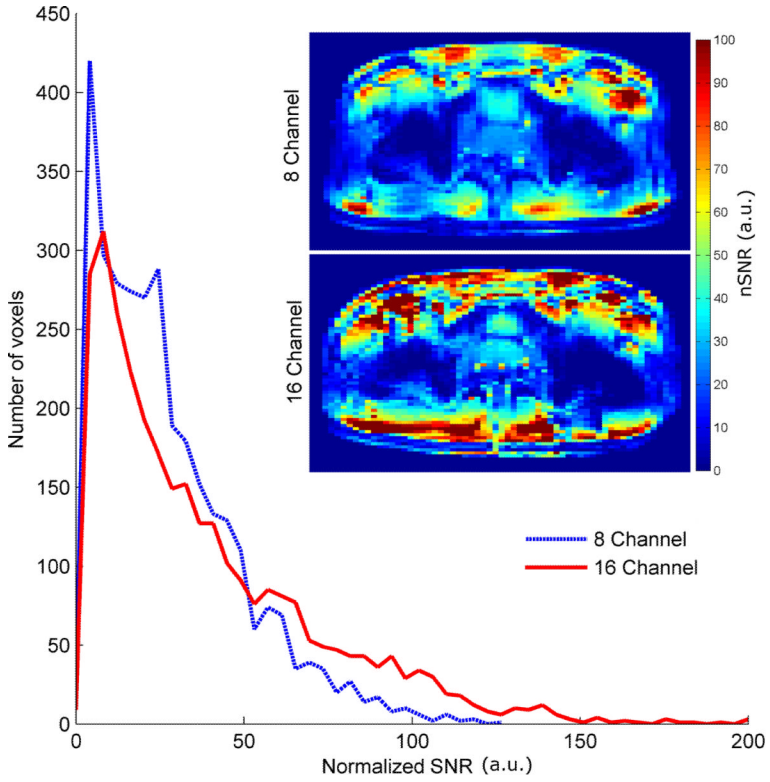

Fig. 5.

Histogram of all nSNR values derived from the long repetition time GRE acquisition for both the eight- and sixteen-channel arrays. Both of the nSNR images used to generate the histrogram are shown as insets. Both the images and histogram demonstrate the increased receive performance of the sixteen-channel array in the periphery. This data was acquired to better demonstrate the receive performance across the torso as it is independent of T_1 weighting.

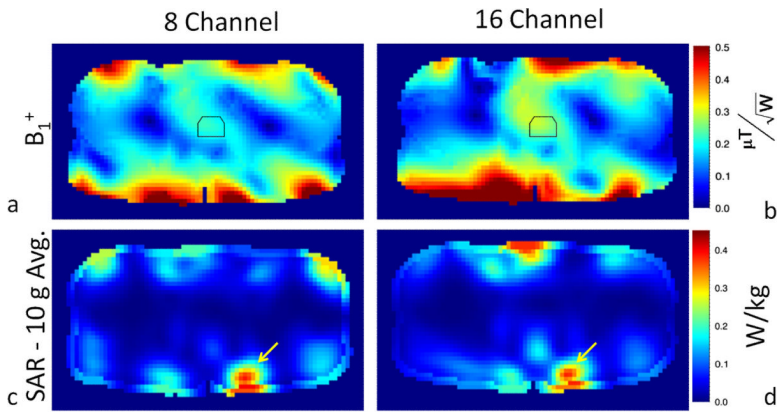

Fig. 6.

Simulation results for the (a) eight- and (b) sixteen-channel arrays in terms of transmit B_1 normalized by input power. 10 gram averaged SAR normalized by input power for the (c) eight-and (d) sixteen-channel arrays. The location of maximum SAR in each of the images (c–d) is indicated with a yellow arrow and the value's maximum local SAR normalized to 1 W input power are given in table 2.

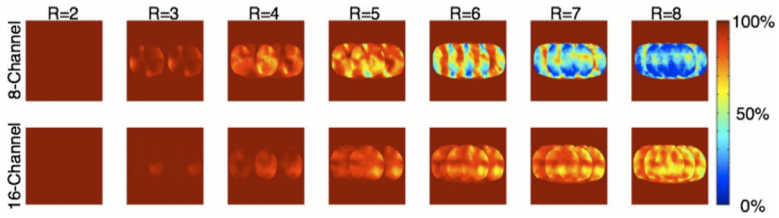

Fig. 7.

Experimental 1/g-factor maps in an axial slice at the level of the prostate in the human torso for the eight- and sixteen-channel arrays. One-dimensional reduction factors from 2 to 8 in the left-right direction are shown. The sixteen-channel array displays substantial improvements in g-factors over the eight-channel. For example, at a reduction factor of 4, the eight-channel array has a mean reduction factor of 1.48 with a maximum g-factor of 2.43 while the sixteen-channel has a mean g-factor of 1.11 and a maximum g-factor of 1.36.

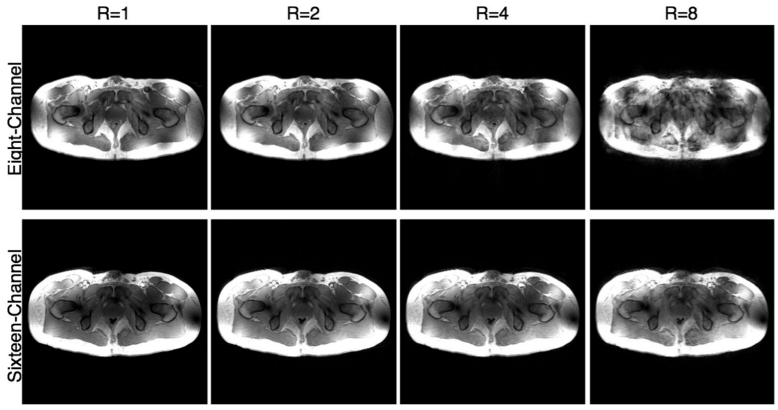

Fig. 8.

From left to right, GRAPPA reconstructed 3D FLASH images of the full dataset (R=1) and at reduction factors of two (R=2), four (R=4) and eight (R=8) are shown for both coils. All reductions are 1-D in the left-right direction. The acquisition time for the full field of view image was 32 s and only 4 s for the eight-fold reduction.

Table 1

The unloaded and loaded Q values, as well as, the isolation between nearest neighboring (NN) and next nearest neighbors (NNN) coils for both the unloaded and loaded case.

	Q_U	Q_L	Q_{ratio}	S_{21U} NN	S_{21L} NN	S_{21U} NNN	S_{21L} NNN
Single Channel	143	23	6.2				
Eight-channel	125 ± 13	32±5	3.9	−15 dB	−20 dB	−12 dB	−22 dB
Sixteen-channel	127 ± 15	34±6	3.8	−21 dB	−26 dB	−11 dB	−25 dB

Table 2

The simulated and experimental transmit efficiency (in the prostate) along with global and local peak SAR for the both the eight- and sixteen-channel arrays. In all cases, B_1^+ shimming was used to increase the transmit efficiency in the prostate.

		B_1^+			Local (10 g avg.)		Whole Body	
Array		Mean $\mu T/W^{0.5}$	Std Dev $\mu T/W^{0.5}$	% inhomo.	SAR/W	$SAR/(B_1^+)^2$	SAR/W	$SAR/(B_1^+)^2$
8	Simulation	0.202	0.018	9%	0.355	8.70	0.008	0.188
	in vivo	0.169	0.017	10%	-	-	-	-
16	Simulation	0.267	0.022	8%	0.340	4.77	0.009	0.119
	in vivo	0.206	0.025	12%	-	-	-	-

Table 3

Experimental and simulated g-factors for the eight-channel array at 7T(left) and the simulated g-factors at 3T (right).

			7T				3T	
			Anterior-Posterior					
Reduction			In vivo		Model		Model	
			1	2	1	2	1	2
Left-Right	1	mean	1.00	1.02	1.00	1.01	1.00	1.00
		max	1.00	1.23	1.00	1.04	1.00	1.03
	2	mean	1.03	1.06	1.01	1.02	1.04	1.04
		max	1.25	1.30	1.07	1.08	1.14	1.15
	3	mean	1.18	1.24	1.12	1.14	1.16	1.18
		max	1.71	1.83	1.47	1.54	1.48	1.51
	4	mean	1.48	1.58	1.25	1.31	1.27	1.36
		max	2.43	2.70	2.04	2.24	1.58	2.26

Table 4

Experimental and simulated g-factors for the sixteen-channel array at 7T(left) and the simulated g-factors at 3T (right).

			7T				3T	
			Anterior-Posterior					
Reduction			In vivo		Model		Model	
			1	2	1	2	1	2
Left-Right	1	mean	1.00	1.03	1.00	1.01	1.00	1.00
		max	1.00	1.23	1.00	1.05	1.00	1.05
	2	mean	1.01	1.05	1.01	1.02	1.03	1.04
		max	1.10	1.30	1.06	1.09	1.17	1.17
	3	mean	1.03	1.09	1.05	1.07	1.14	1.15
		max	1.14	1.40	1.32	1.35	1.40	1.43
	4	mean	1.11	1.21	1.10	1.12	1.25	1.29
		max	1.36	1.65	1.35	1.39	1.71	1.81
	5	mean	1.19	1.38	1.16	1.19	1.41	1.50
		max	1.63	2.10	1.39	1.53	2.00	2.28
	6	mean	1.27	1.60	1.33	1.27	1.68	1.87
		max	1.84	2.73	1.59	2.02	2.43	3.10
	7	mean	1.38	1.98	1.31	1.41	2.16	2.55
		max	2.13	3.98	1.59	2.34	3.38	4.97
	8	mean	1.58	3.17	1.52	1.72	2.98	3.93
		max	2.78	>10	2.54	3.44	5.99	>10